

Figure 4 Point spread function (PSF) at point $(-2.5 \text{ cm}, 2.5 \text{ cm})$

very high, at point $(0, 0)$ and point $(-2.5 \text{ cm}, 2.5 \text{ cm})$, the resolutions are nearly the same. This implies that even when the imaging object is located far from the rotating center, it is possible to visually reconstruct the profile of the object. The numerical results show that the higher center frequency f_0 may yield better resolution if the sweep frequency range is fixed (for example, 10 GHz).

5. CONCLUSION

A novel theory about near-field microwave imaging has been proposed and a near-field microwave diversity imaging system has been constructed, which includes data acquisition, imaging process, and imaging display. This paper mainly focused on a theoretical investigation of the imaging process for the turntable mode. We derived the imaging function in both the space and spectrum domains. The imaging function is an integral of the backscattering of the object over a given window in the Fourier domain. The imaging resolution of this system, which depends on the sweep frequency and rotatory angle ranges (so-called frequency- and angle-diversity), was then studied. The theoretical results indicated that the PSF of the imaging system for the practical case could infinitely approach that of the ideal case when $B \rightarrow \infty$, namely, the Dirac- δ function. Further investigation is in progress and relevant developments will be reported soon.

REFERENCES

1. M.R. Tofghi and A.S. Daryoush, Near field microwave brain imaging, *Electron Lett* 37 (2001), 807–808.
2. I.T. Rekanos, M.S. Efraimidou, and T.D. Tsibouki, Microwave imaging: inversion of scattered near-field measurements, *IEEE Trans Magnetics Mag* 37 (2001), 3294–3297.
3. J. Ma and H. Wu, Spherical back-projection method imaging for perfectly conducting objects, *Acta Electronica Sinica* 24 (1995), 26–29.
4. J. Ma, Y. Jiao, and N. Mao, A new technique for image reconstruction from near-field backscattering, *IEEE AP-S Dig* (1998), 689–701.
5. T.H. Chu and D.B. Lin, Microwave diversity imaging of perfectly conducting objects in the near-field region, *IEEE Trans Microwave Theory Tech* 39 (1991), 480–487.
6. H.J. Li and F.L. Lin, Near-field imaging for conducting objects, *IEEE Trans Antennas Propagat AP* 39 (1991), 600–605.

© 2003 Wiley Periodicals, Inc.

ACCURATE COMPUTATION OF VECTOR POTENTIALS IN LOSSY MEDIA

Swagato Chakraborty and Vikram Jandhyala

Department of Electrical Engineering
University of Washington
Seattle, WA 98195

Received 13 August 2003

ABSTRACT: This paper presents an accurate formulation and integration scheme for computing vector potential interactions due to linear basis functions in lossy conducting media over wide frequency ranges. The emphasis is on an approach that is broadband and works both at high-frequency surface impedance limits and at low-frequency volumetric current flow limits. The method can be interpreted as a step towards a surface-only formulation for an integral-equation-based broadband characterization. © 2003 Wiley Periodicals, Inc. *Microwave Opt Technol Lett* 36: 359–363, 2003; Published online in Wiley InterScience (www.interscience.wiley.com). DOI 10.1002/mop.10764

Key words: vector potentials; method of moments; conducting media; skin effects; surface formulation

1. INTRODUCTION

Modeling the interior problem associated with a lossy conductor is of particular importance in the ultra-wideband frequency-domain modeling of structures such as interconnects and packages. This is specifically of interest at frequencies where the cross sections of conductors are smaller than their skin depths. In such cases, surface impedance approximations break down, and recourse is normally taken to explicit volumetric formulations.

This paper presents a step towards surface-only wideband modeling of interconnects and packages through an exact formulation and accurate numerical integration scheme for efficiently computing highly damped vector potentials in lossy conductors. The presented method is general in terms of geometries, frequencies, material parameters, and relative separation and orientation of source and observer regions. The motivation behind the presented approach is that a coupled integral equation formulation, linking an exterior homogeneous medium problem to an interior lossy medium problem, is required in order to correctly predict electromagnetic behavior of conductors in specific frequency bands. As line widths and heights of interconnects become smaller, and as progressively smaller devices and structures are integrated at the package and chip levels, the underlying complex analyses cannot be handled by an *ad hoc* mixing of surface and volume formulations, and seamless wideband formulations become imperative.

2. VECTOR POTENTIALS IN LOSSY CONDUCTING MEDIA

Computing the electric field in a lossy medium requires computation of scalar and vector potentials. The scalar potential computation has been studied previously in [1], and this paper deals with the computation of vector potentials for arbitrarily located sources and observation points. The vector potential \mathbf{A} is given by

$$\mathbf{A}(\mathbf{r}) = \frac{\mu}{4\pi} \int_{S'} \frac{e^{-jk|\mathbf{r}-\mathbf{r}'|}}{|\mathbf{r}-\mathbf{r}'|} \mathbf{J}(\mathbf{r}') ds', \quad (2.1)$$

where \mathbf{r} and \mathbf{r}' are the position vectors of the observation point and of an arbitrary point in the source region, respectively, and S' denotes the conductor surface. The source current density is de-

noted by \mathbf{J} , and k is the wave number in the lossy medium given by

$$k = \omega \sqrt{\mu_0 \mu_r \epsilon_0 \left(\epsilon_r + \frac{\sigma}{j\omega \epsilon_0} \right)}, \quad (2.2)$$

where σ is the conductivity of the lossy medium, μ_0 and ϵ_0 represent the free-space permeability and permittivity, respectively, and $\omega = 2\pi f$, where f is the frequency of interest. Also, μ_r and ϵ_r represent the relative permeability and relative permittivity of the lossy medium, including magnetic and dielectric losses; typically, these are both equal to 1 for metallic conductors. The popular triangle-pair-based Rao–Wilton–Glisson (RWG) functions [2] are used to represent $\mathbf{J}(\mathbf{r}')$, wherein current is modeled by piecewise linear vector functions. The vector potential integral computation (2.1) is replaced by integrals of the form

$$\iint_T \frac{\boldsymbol{\rho} e^{-jk|\mathbf{R}|}}{|\mathbf{R}|} ds', \quad (2.3)$$

where $\mathbf{R} = \mathbf{r} - \mathbf{r}'$, and $\boldsymbol{\rho}$ denotes a vector from the node opposite the edge of interest in triangle T to \mathbf{r}' . The distinction from the corresponding integrals in the exterior equivalent problem is that the wave-vector is complex and may lead to strong exponential decays in the integrands, depending upon the frequency of interest.

3. PREVALENT METHODS FOR LOSSY CONDUCTING MEDIA

Existing techniques for lossy media computations involve the use of polar coordinate transformations. This has been accomplished for the evaluation of the scalar Green's function [1], and in the context of lossless media [3, 4]. The self-term for the vector potential integral has been computed using a polar coordinate transformation [5], and the method presented therein is extendable to observation points in the plane of the source triangle. This precludes the important case of observation at a near-singular point located above or below the source triangle, as often occurs in thin conductors. In this work, the restrictions on observer location are lifted and a general computation of vector potentials due to RWG functions in lossy conducting media is performed.

4. FREQUENCY DEPENDENCE OF VECTOR POTENTIALS IN CONDUCTING MEDIA

The sparsity of the method of moments (MoM) matrix corresponding to Green's function interactions in lossy conducting media is highly frequency-dependent. At sufficiently high frequencies, where conductor cross-sections are significantly larger than skin depth, the surface impedance approximation is very accurate. Consequently, the MoM matrix based on the RWG and testing functions is nearly diagonal, with only interactions between overlapping functions being non-zero. As the frequency is reduced, the exact exponential decay of the potentials is apparent, and there is a distance beyond which the interactions are numerically zero (for example, in double precision). Further lowering of frequency yields a full matrix, with an exponential decay with distance. Finally, at very low frequencies, where the conductor cross-sections are significantly smaller than the skin depth, the matrix is dense with a mild exponential decay. The formulation and integration scheme presented here is intended for wideband vector potential in lossy conducting media, that is, to compute the interactions over the entire frequency range as described above.

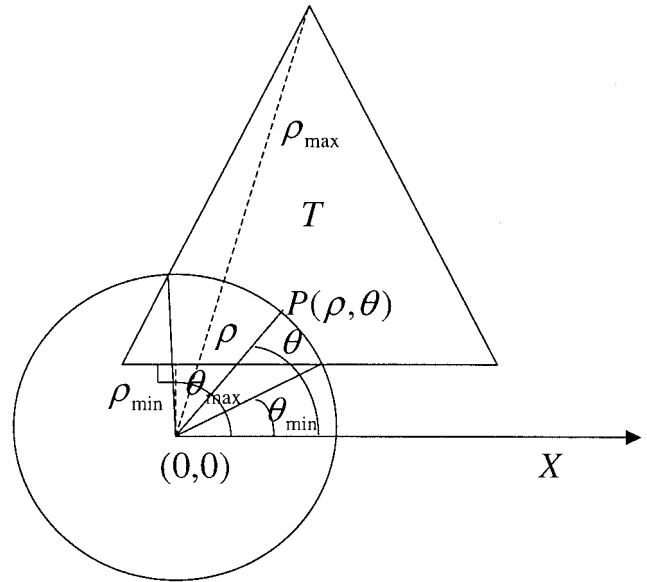


Figure 1 Triangle T in transformed coordinates, with the projection of the observation point as the origin

5. FORMULATION OF THE INTEGRALS AND NUMERICAL INTEGRATION SCHEME

The vector potential integral $\mathbf{G}_{V_{\text{vect}}}$ due to RWG functions can be written in polar coordinates as

$$\mathbf{G}_{V_{\text{vect}}}(\mathbf{r}) = \hat{\mathbf{x}} \int_T \frac{\rho e^{-jk \sqrt{\rho^2 + d^2}}}{\sqrt{\rho^2 + d^2}} \rho \cos(\theta) d\rho d\theta + \hat{\mathbf{y}} \int_T \frac{\rho e^{-jk \sqrt{\rho^2 + d^2}}}{\sqrt{\rho^2 + d^2}} \rho \sin(\theta) d\rho d\theta, \quad (5.1)$$

where it is assumed, for ease of discussion, and without loss of generality, that the triangle T (Fig. 1) lies in the $x - y$ plane. In the above equation, the distance d is the height of the observation point from the plane of T , and the distance ρ is the separation of source points in T from the projection of the observation point onto the plane of T .

For the case when the observation point is in the plane of T , d equals zero and it is possible to carry out the integration as in [5] to yield

$$\mathbf{G}_{V_{\text{vect}}}(\mathbf{r}) = \hat{\mathbf{x}} \int_T \rho e^{-jk\rho} d\rho \cos(\theta) d\theta + \hat{\mathbf{y}} \int_T \rho e^{-jk\rho} \sin(\theta) d\theta. \quad (5.2)$$

Existing work reported in the literature [5] focuses on the self-term computation, and the results can readily be extended to the in-plane observation case, but do not apply to the general case of arbitrarily located and oriented basis and testing functions at all frequencies. This is due to the lack of a closed-form expression for one-dimensional integration with respect to ρ in (5.1) for $d \neq 0$. In order to lift this restriction and to enable a one-dimensional analytic integration followed by a one-dimensional numerical integration for (5.1), the integration order needs to be reversed compared to existing work for scalar and in-plane cases; integra-

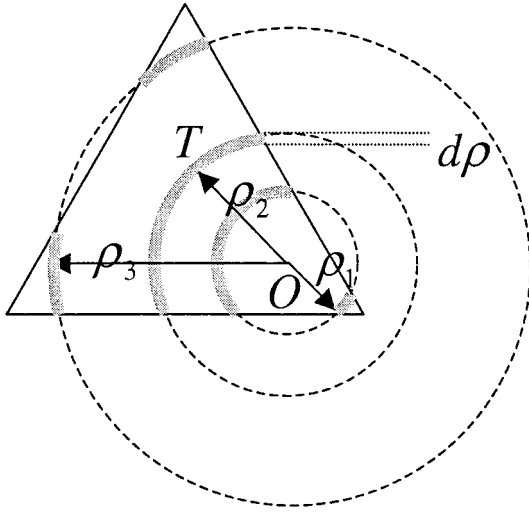


Figure 2 Region of integration for specific values of ρ for a triangle T . The origin for determining distances is the projection O of the observation point on the plane of T

tion over θ is performed analytically followed by a numerical integration over ρ :

$$\mathbf{G}_{vect}(\mathbf{r}) = \hat{\mathbf{x}} \int_{\rho_{\min}}^{\rho_{\max}} \frac{\rho^2 e^{-jk\sqrt{\rho^2+d^2}}}{\sqrt{\rho^2+d^2}} [\sin(\theta)]_{\theta_{\min}}^{\theta_{\max}} d\rho + \hat{\mathbf{y}} \int_{\rho_{\min}}^{\rho_{\max}} \frac{\rho^2 e^{-jk\sqrt{\rho^2+d^2}}}{\sqrt{\rho^2+d^2}} [-\cos(\theta)]_{\theta_{\min}}^{\theta_{\max}} d\rho. \quad (5.3)$$

In the above equation, $[\frac{(-\cos \theta)}{\sin \theta}]_{\theta_{\min}}^{\theta_{\max}}$ is required as a function of ρ . For a given ρ , when the integration points lie inside the triangle for all values of θ , the multiplying function becomes $\int_0^{2\pi} (\frac{\cos \theta}{\sin \theta}) d\theta$, which integrates to zero. Also, for $\forall(\rho, \theta) : P(\rho, \theta) \notin T$, the integral is zero, where $P(\rho, \theta)$ denotes a point having coordinate (ρ, θ) . Hence, the limits are obtained for the piecewise boundaries, where $P(\rho, \theta) \in T$, as shown in Figure 2. To obtain the limits on θ as a function of ρ , the reference coordinate system in which T lies in the $x - y$ plane is translated so that the projection of the observation point onto the plane of T defines the origin (Fig. 1). The intersection of a circle of constant ρ with the sides of the triangle determines the limits of integration in θ . The expression $[\frac{(-\cos \theta)}{\sin \theta}]_{\theta_{\min}}^{\theta_{\max}}$ is evaluated for a given ρ to arrive at the final form of the one-dimensional integral

$$\mathbf{G}_{vect}(\mathbf{r}) = \hat{\mathbf{x}} \int_{\rho_{\min}}^{\rho_{\max}} \Psi_1(\rho) d\rho + \hat{\mathbf{y}} \int_{\rho_{\min}}^{\rho_{\max}} \Psi_2(\rho) d\rho, \quad (5.4a)$$

where

$$\Psi_1(\rho) = \frac{\rho^2 e^{-jk\sqrt{\rho^2+d^2}}}{\sqrt{\rho^2+d^2}} (\sin \theta_{\max}(\rho) - \sin \theta_{\min}(\rho)) \quad (5.4b)$$

and

$$\Psi_2(\rho) = \frac{\rho^2 e^{-jk\sqrt{\rho^2+d^2}}}{\sqrt{\rho^2+d^2}} (-\cos \theta_{\max}(\rho) + \cos \theta_{\min}(\rho)). \quad (5.4c)$$

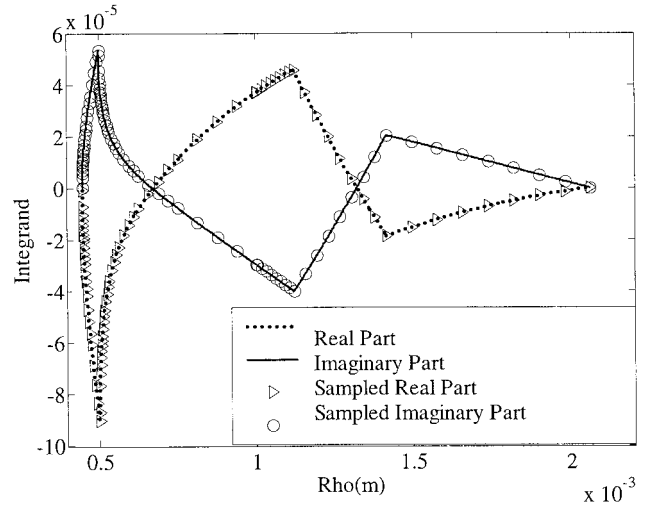


Figure 3 Behavior of $\psi_1(\rho)$ and adaptive sampling for the non-self-term integral, for a triangle with vertices $(\alpha, -\alpha, \alpha)$, $(\alpha, \alpha/2, \alpha)$, $(-\alpha, \alpha/2, \alpha)$, and observation point located at $(0, 0, 2\alpha)$, where $\alpha = 0.001$ m, at a frequency of 1 KHz, with $\sigma = 5.8 \times 10^7$ S/m. The stopping threshold resulted in a relative integration error of 2.59×10^{-5}

The one-dimensional integrals arising above are evaluated using an adaptive integration technique. In general, the integrands appear as segmented piecewise functions, each of which has a smooth variation in its domain. Within each segment, a recursive adaptive integration is carried out. A binary segment split is performed, and the resultant integration value from a 5th-order Newton-Cotes formula (Bode's rule) [7] over the two sub-segments is compared to the integration value obtained with the same integration rule over the un-split segment. If the relative change in integration value is larger than a prespecified threshold, then the binary split continues recursively. In addition, a global threshold based on the contribution of a sub-segment to the total integral is used as a stopping criterion.

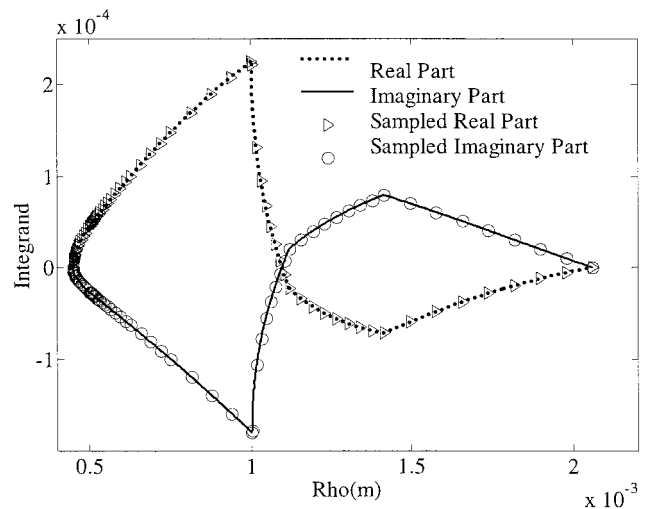


Figure 4 Behavior of $\psi_2(\rho)$ and adaptive sampling for the non-self-term integral, for a triangle with vertices $(\alpha, -\alpha, \alpha)$, $(\alpha, \alpha/2, \alpha)$, $(-\alpha, \alpha/2, \alpha)$, and observation point located at $(0, 0, 2\alpha)$, where $\alpha = 0.001$ m, at a frequency of 1 KHz, with $\sigma = 5.8 \times 10^7$ S/m. The stopping threshold resulted in a relative integration error of 2.59×10^{-5}

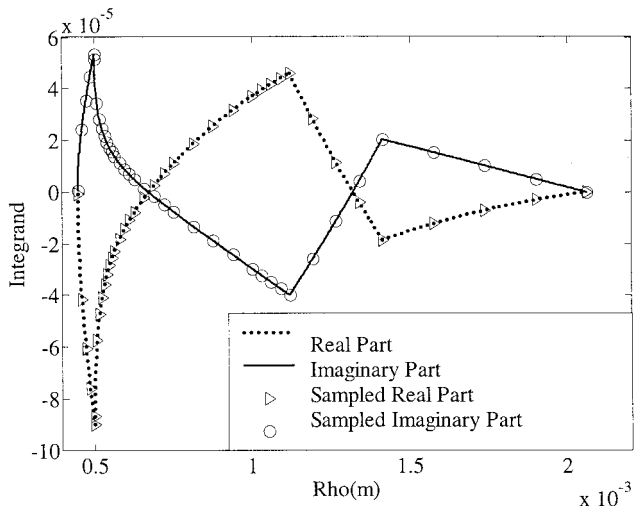


Figure 5 Behavior of $\psi_1(\rho)$ and adaptive sampling for the non-self-term integral, for a triangle with vertices $(\alpha, -\alpha, \alpha)$, $(\alpha, \alpha/2, \alpha)$, $(-2\alpha, \alpha/2, \alpha)$, and observation point located at $(0, 0, 2\alpha)$, where $\alpha = 0.001$ m, at a frequency of 1 KHz, with $\sigma = 5.8 \times 10^7$ S/m. The stopping threshold resulted in a relative integration error of 2.23×10^{-3}

6. NUMERICAL SIMULATION AND VALIDATION

The real and imaginary parts of the two integrands $\psi_1(\rho)$ and $\psi_2(\rho)$ in Eq. (5.4) are shown in Figures 3 and 4 for a non-planar case. Also shown is the sampling based on the adaptive integration, within each segment of the integration, for $O(10^{-5})$ error in integration accuracy. The location of quadrature points can be intuited by the variation and curvature of the integrands, especially for lower accuracy cases; the sampling points are shown in Figures 5 and 6 for the same integrands for a higher error of $O(10^{-3})$ in integration accuracy.

The nature of the vector potential at both low frequencies and very high frequencies lends itself to simpler computation schemes, namely, singularity extraction [6] and Gaussian quadrature (typically 7 point) [7], and surface impedance forms, respectively. As

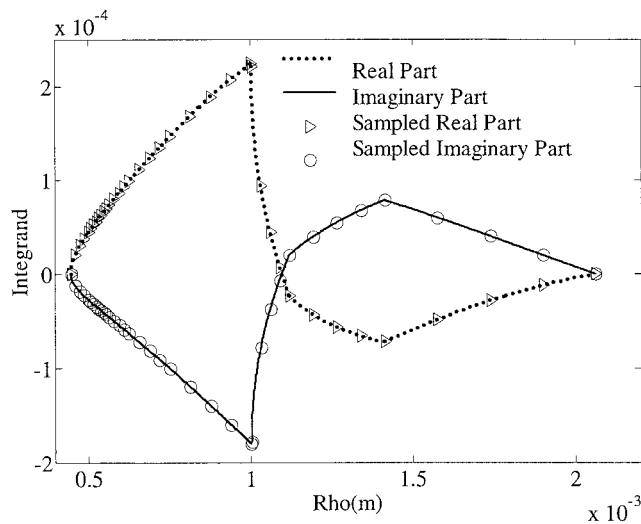


Figure 6 Behavior of $\psi_2(\rho)$ and adaptive sampling for the non-self-term integral, for a triangle with vertices $(\alpha, -\alpha, \alpha)$, $(\alpha, \alpha/2, \alpha)$, $(-2\alpha, \alpha/2, \alpha)$, and observation point located at $(0, 0, 2\alpha)$, where $\alpha = 0.001$ m, at a frequency of 1 KHz, with $\sigma = 5.8 \times 10^7$ S/m. The stopping threshold resulted in a relative integration error of 2.23×10^{-3}

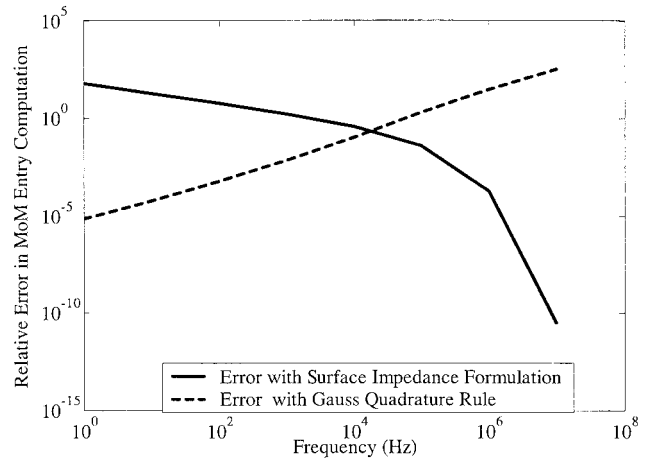


Figure 7 Validation and comparison of the proposed method with singularity extraction and a 7-point Gaussian quadrature rule for low frequencies and surface impedance for high frequencies. The compared value is the self-patch interaction for a triangle with vertices $(0.1, -0.1, 0)$ cm, $(0.1, 0.05, 0)$ cm, $(-0.2, 0.05, 0)$ cm, with $\sigma = 5.8 \times 10^7$ S/m

a self-consistency check, the integration scheme constructed in this paper is compared against these standard methods. The results are shown in Figure 7, for a specific self-term case with $\sigma = 5.8 \times 10^7$ S/m. As can be seen, as the frequency increases, the relative error between the proposed integration method and surface impedance approximations drastically fall to very low values. Similarly, the proposed scheme shows very good agreement with standard Gaussian quadrature and singularity extraction at low frequencies. At the same time, the need for the accurate integration scheme is self-evident in the intermediate band of frequencies. The self-term was used in order to be able to compare against surface impedance. A similar comparison for the non-self-term case is shown in Figure 8 versus standard singularity extraction and Gaussian quadrature. In this case, the need for accurate integration is highlighted, since the standard singularity extraction and Gaussian quadrature starts performing poorly as the frequency is increased.

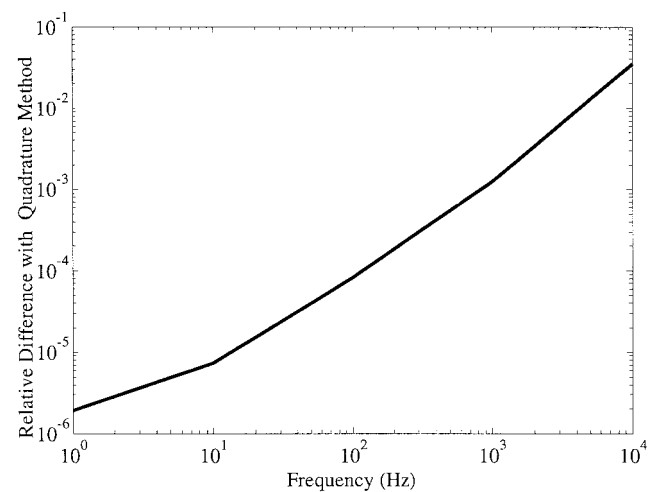


Figure 8 Comparison of the proposed method with singularity extraction and a 7-point Gaussian quadrature rule for a non-self-patch interaction, where the source triangle has vertices $(0.1, -0.1, 0)$ cm, $(0.1, 0.05, 0)$ cm, $(-0.2, 0.05, 0)$ cm, and the observation point is at $(0, 0, 0.1)$ cm, with $\sigma = 5.8 \times 10^7$ S/m

TABLE 1 Validation of the Proposed Method with the Existing Technique in [5] for In-Plane Observation Points

ρ -cm	$G_{Vect}\hat{x}$		$G_{Vect}\hat{y}$		Relative Error
	Existing Method in [5]	Proposed Method	Existing Method in [5]	Proposed Method	
0	$10^{-6} \times 0.126930 - 0.024078i$	$10^{-6} \times 0.126853 - 0.024049i$	$10^{-6} \times -0.000174 + 0.002200i$	$10^{-6} \times -0.000176 + 0.002192i$	6.41×10^{-4}
0.05	$10^{-6} \times -0.434146 + 0.261252i$	$10^{-6} \times -0.4341153 + 0.261176i$	$10^{-6} \times -0.107124 + 0.019400i$	$10^{-6} \times -0.107093 + 0.019376i$	1.73×10^{-4}
0.1	$10^{-6} \times 0.941456 + 0.494869i$	$10^{-6} \times 0.941245 + 0.494778i$	$10^{-6} \times -0.118088 + 0.027149i$	$10^{-6} \times -0.118055 + 0.027132i$	2.17×10^{-4}
0.15	$10^{-6} \times 0.796986 + 0.617191i$	$10^{-6} \times 0.796777 + 0.617102i$	$10^{-6} \times -0.073881 + 0.026486i$	$10^{-6} \times -0.073800 + 0.026438i$	2.42×10^{-4}

The source triangle has vertices (0.1, -0.1, 0) cm, (0.1, 0.05, 0) cm, (-0.2, 0.05, 0) cm, and the observation point is parameterized as (ρ , 0, 0). The frequency is 1 KHz, with $\sigma = 5.8 \times 10^7$ S/m.

Finally, the proposed scheme is compared for accuracy versus an existing method for the special case of in-plane observation. Table 1 shows the relative errors between the new method and the method in [5] for the components of the vector integral, for different source-observer distances. As can be seen, in all cases relative errors smaller than 10^{-3} are obtained.

7. CONCLUSION

A formulation and integration scheme to compute vector potentials in a lossy conducting medium was presented in this paper. This general method compares well in terms of accuracy with existing methods with restricted applicability, is error-controllable, and can be used for vector potential computations at all frequencies in conducting media, for arbitrarily located and oriented source and basis functions. Ongoing work focuses on similar formulation and integration rules for Green’s function integrals arising in the modeling of lossy dielectric and lossy magnetic structures, extension of the method to polygonal regions, and a two-region surface integral equation formulation for wideband modeling of inductances and impedances of realistic interconnects and package structures.

ACKNOWLEDGMENTS

This work was supported in part by DARPA-MTO NeoCAD grant N66001-01-1-8920, NSF-CAREER grant ECS-0093102, NSF-SRC Mixed-Signal Initiative grant CCR-0120371, and by a grant from Ansoft Corporation. The authors would like to thank Dr. John Rockway, SSC San Diego, and Dr. J. Eric Bracken, Ansoft Corporation, Pittsburgh, for helpful discussions.

REFERENCES

1. Z. Zhu, J. Huang, B. Song, and J. White, Improving the robustness of a surface integral formulation for wideband impedance extraction of 3D structures, Proc Int Conf Computer Aided Design (2001), 592–597.
2. S.M. Rao, D.R. Wilton, and A.W. Glisson, Electromagnetic scattering by surfaces of arbitrary shape, IEEE Trans Antennas Propagat 30 (1982), 409–418.
3. M. Gimersky, S. Amari, and J. Bornemann, Numerical evaluation of the two-dimensional generalized exponential integral, IEEE Trans Antennas Propagat 44 (1996), 1422–1425.
4. J.K.H. Gamage, Efficient method of moments for compact large planar scatterers in homogeneous medium, Proc 11th Int Conf Antennas Propagat 480 (2001), 741–744.
5. L. Rossi and P.J. Cullen, On the fully numerical evaluation of the linear-shape function times the 3-D Green’s function on a planar triangle, IEEE Trans Microwave Theory Techniques 47 (1999), 398–402.
6. R.D. Graglia, On the numerical integration of the linear shape function times the 3-D Green’s function or its gradient on a planar triangle, IEEE Trans Antennas Propagat 41 (1993), 1448–1455.
7. M. Abramowitz and I. Stegun, Handbook of Mathematical Functions, Chapter 25, Dover, New York, 1970.

© 2003 Wiley Periodicals, Inc.

DESIGN OF STEERABLE NON-UNIFORM LINEAR ARRAY GEOMETRY FOR SIDE-LOBE REDUCTION

Ji-Hoon Bae,¹ Kyung-Tae Kim,² Joon-Ho Lee,¹ Hyo-Tae Kim,³ and Jae-Ick Choi¹

¹ Advanced Radio Department
Radio and Broadcasting Research Laboratory
Electronics and Telecommunication Research Institute
151 Gajeong-dong, Yuseong-gu
Daejeon, 305-350, Korea

² Dept. of Electrical Engineering and Computer Science
Yeungnam University
214-1 Dae-dong, Kyongsan
Kyungbuk, 712-749, Korea

³ Electrical and Computer Engineering Division
Pohang University of Science and Technology
San 31 Hyoja-dong, Nam-gu, Pohang
Kyungbuk, 790-784, Korea

Received 12 August 2002

ABSTRACT: In this paper, we present a pattern synthesis method of non-uniform linear array antennas for simultaneous reduction of the side-lobe level and pattern distortion during beam steering. To achieve these two requirements, the positions of linear array elements are adjusted using the Gauss–Newton method. It is shown that the proposed method can significantly reduce pattern distortion as well as the side-lobe level, although the beam direction is scanned. © 2003 Wiley Periodicals, Inc. Microwave Opt Technol Lett 36: 363–367, 2003; Published online in Wiley InterScience (www.interscience.wiley.com). DOI 10.1002/mop.10765

Key words: antenna array pattern synthesis; non-uniform spacing; optimization technique; side-lobe reduction

1. INTRODUCTION

In the field of antenna array pattern synthesis, the side-lobe level of an array radiation pattern can be reduced by appropriately changing inter-element spacing, namely, by applying a non-uniformly spaced array [1–4]. Of course, the desired low side-lobe level can be achieved by optimizing the amplitudes and phases of excited array elements with uniform spacing. However, this synthesis method degrades total radiation power efficiency due to amplitude tapering, which requires a complicated feed system. Therefore, it is preferable to use a non-uniformly spaced array to improve the side-lobe level, while maintaining total radiation power efficiency. The non-uniform linear array (NULA) can reduce inner side-lobes (nearby side-lobes from the main beam), whereas it may increase outer side-lobe levels [1]. Because of this phenomenon, its radiation pattern with scanning includes undesirable large side-lobes in the visible region, whose levels can be higher than the first side-lobe level. To overcome this problem, an optimization technique is adopted to reduce both the inner side-